Efficient DEM calibration of AM powders using a rotating drum through Froude number scaling

Progress in Additive Manufacturing
https://doi.org/10.1007/s40964-026-01627-6

RESEARCH

Efficient DEM calibration of AM powders using a rotating drum through Froude number scaling

Negar Sani[1] · Johannes Quist[1,2] · Sofia Kazi[2] · Gowtham Soundarapandiyan[2] · Gustav Kettil[1] · Laura Cordova[2] · Eduard Hryha[2] · Fredrik Edelvik[1]

Received: 25 June 2025 / Accepted: 25 February 2026

Abstract Powder qualification in additive manufacturing (AM) is a complex process, requiring extensive know-how to ensure that powder properties are suitable for a specific hardware solution and AM process. This qualification is typically performed through trial-and-error methods, which are costly, time-consuming, and provide little insight into powder behavior. Without a deeper understanding of powder properties, opportunities for optimizing either the powder itself or the recoating mechanism remain unexplored. The Discrete Element Method (DEM) offers a solution by enabling virtual powder characterization and parameter optimization. A method is proposed for calibrating a DEM model of AM powder that incorporates the real particle size distribution by properly scaling the system geometry rather than relying on coarse-graining techniques. A surrogate model-based calibration approach is employed to adjust DEM model parameters simultaneously, capturing their interdependencies and combined effects. A revolution device serves as the experimental reference for the calibration process. To reduce computational costs, a scaled-down simulation setup is introduced while maintaining dimensions significantly larger than the particle size. The calibration method is demonstrated using two widely used AM powders: Inconel 718 and Ti-6Al-4V (Ti64). The geometry down-scaling approach is validated through simulations with the calibrated model across various scaling factors. Additionally, the simulations provide insights into avalanche progression and size segregation in the revolution device. The contribution of this work is a calibration strategy for DEM-based powder modeling in AM that explicitly accounts for the real particle size distribution and is supported by validation in the revolution device. This provides a basis for reliable representation of powders in rotating drum flow, while future work should clarify the extent to which the calibrated state corresponds to the granular dynamical response during recoating.

Graphic abstract

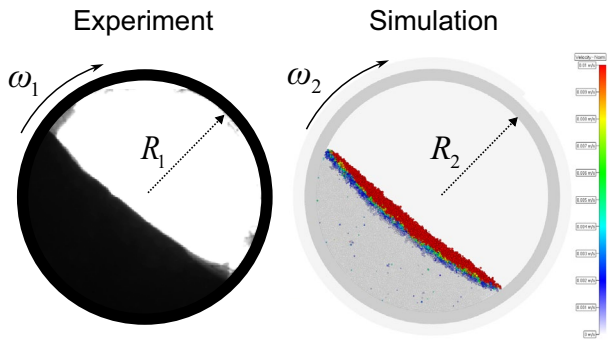

$$Fr = \frac{\omega^2 R}{g}$$

Keywords DEM · Additive manufacturing · Model calibration · Metal powder

Extended author information available on the last page of the article

Published online: 15 April 2026

1 Introduction

Metal additive manufacturing (AM), and in particular Powder Bed Fusion (PBF), relies on thin layers of metal powder to build parts with complex geometries. The characteristics of each deposited powder layer influence the quality of the final part, including composition, grain structure, and the presence of defects [1]. Achieving a uniform layer during recoating depends on both intrinsic powder properties and process parameters such as recoater speed and clearance. The term spreadability is increasingly used to describe this ability to form a consistent powder layer [2, 3].

Optimizing spreading conditions is commonly done experimentally, but this trial-and-error approach is cost- and time-intensive. Numerical simulation offers an alternative, and the Discrete Element Method (DEM) [4] has become the leading approach for modeling powder behavior in PBF. However, the widespread use of DEM in AM has historically been limited by high computational cost. Recent advances in high-performance computing and GPU-accelerated algorithms now make large-scale powder simulations increasingly feasible, enabling virtual process optimization [5, 6].

The development and calibration of a reliable DEM model for the powder material is a crucial first step in virtually investigating spreadability and ensuring accurate results prior to recoating optimization. Several powder properties, such as density, elasticity, Poisson's ratio, and particle size distribution, can be directly measured and implemented in the DEM model. However, direct measurement of inter-particle and particle-tool interaction parameters is challenging. Therefore, these parameters are typically identified through model calibration against the powder's bulk behavior in controlled experiments [7, 8]. Standard setups include angle of repose (AOR) tests, the Hall flow meter, shear cells, and dynamic flow tests using rheometers or revolution drums [9].

When calibrating DEM models using such experimental tests, several considerations are essential. First, the chosen test must represent the relevant flow regime, stress state, and boundary conditions of the target process; otherwise, the calibrated parameters may reproduce the experiment but fail to predict the actual application. Second, the experiment must provide repeatable and robust measurements, since high variability or operator dependence reduces confidence in the resulting parameter set. Third, the test should be practical to reproduce numerically without excessive assumptions or simplifications.

Static AOR tests are popular for their simplicity, but are highly sensitive to setup conditions and material properties, particularly for cohesive powders, often resulting in inconsistent data [8, 10, 11]. In addition, they capture only static behavior and do not reflect the dynamic flow mechanisms relevant to recoating. Rheology-based approaches, such as the FT4 powder rheometer, provide richer data, but are difficult to model realistically due to system complexity. In contrast, the Revolution Powder Analyzer (RPA) drum is well established in AM for evaluating powder flowability, providing steady granular flow, high repeatability, and robust measurement metrics [2, 12, 13]. Its proven performance, combined with a simpler interaction environment and fewer parameters than rheology-based methods, makes it a particularly strong choice for DEM powder model calibration [8, 14, 15].

The calibration process involves reproducing the experimental setup in the simulation environment and adjusting the DEM model parameters until the simulated bulk response matches experimental observations. The number of required simulations, and therefore the computational cost, grows rapidly with the number of parameters to be calibrated. Different strategies can be used to reduce the computational cost by reducing the number of simulations or lowering the duration of individual simulations.

The efficiency of the calibration algorithm in converging to the optimal model parameter values is a critical factor in determining the number of simulations required. A wide variety of methods have been proposed to obtain the calibrated model using different search algorithms [16, 17]. Several studies suggest AI-based approaches to calibrate model parameters [18–20]. Design of Experiment (DOE) is another method to limit the number of simulations needed to obtain calibrated values [21]. This approach employs techniques to generate a distribution of parameter combinations, enabling the isolation of each parameter's impact on the system. DOE can be integrated with interpolation algorithms to construct a mathematical model that predicts system responses based on parameter values. This technique, commonly known as surrogate modeling, is widely used in model calibration [22]. This method focuses on reducing the total number of DEM simulations required, rather than decreasing the runtime of individual simulations.

To reduce the computational time of DEM simulations, methods such as coarse-graining, geometric scaling, and scalping [23] can be applied. Coarse-graining is among the most common approaches, decreasing the number of simulated particles. However, particle size directly influences the fundamental force contributions in DEM, including gravitational forces, adhesion, sliding, and friction, each of which scales differently with particle radius. As a result, modifying particle size alters the balance between force components and thereby changes particle-scale interactions as well as bulk flow behavior. Several studies have analytically investigated and proposed adjustments for the effect of up-scaling on parameters calibrated using coarse-graining [24–26].

Many AM process parameters, such as recoater blade clearance, and process outcomes, such as powder layer homogeneity and thickness, depend on true particle size representation. Therefore, a DEM model with real-size particles is essential for virtual recoating process parameter optimization in AM. Consequently, calibration should also be performed using the true particle size distribution.

In this study, we develop a method to calibrate a DEM powder model using the real particle size distribution of the material. A revolution device is adopted as the experimental reference setup, and a geometry down-scaling approach, based on preservation of the Froude number, is applied to reduce the computational cost while ensuring that the dimensions of the setup remain significantly larger than the particle size. This Froude-based down-scaling is adopted as an extension of established scaling concepts into the context of AM powder calibration.

DOE is used to generate input parameter combinations for studying first- and second-order sensitivity of parameters on system responses. A surrogate model is developed and evaluated based on these results and is used to formulate the calibration optimization objective function. An optimization algorithm is subsequently used to calibrate the DEM model by determining the parameter set that minimizes the discrepancy between surrogate model predictions and experimental data. Calibration is performed by adjusting the DEM parameters until the simulated break, rest, and avalanche energy curves agree with their experimentally measured counterparts. While avalanche energy in the RPA is not a direct measure of spreading, it is a reasonable proxy for capturing key aspects of granular dynamics relevant to recoating, though further work is needed to establish the exact correspondence.

The calibration method is demonstrated using two representative Electron Beam PBF (PBF-EB) AM alloys, Inconel 718 and Ti-6Al-4V (Ti64). Finally, the down-scaling approach is assessed by running simulations using the calibrated model with various scaling factors. Lastly, insight into the size segregation progression in the RPA is presented.

2 Methodology

2.1 Materials

The AM powders used in the calibration process are Inconel 718 and Ti-6Al-4V (Ti64), both commonly employed in PBF-EB. The particle size distribution is measured by laser diffraction using a Mastersizer 3000 instrument (Malvern Panalytical, UK). The particle size distributions are reported in Table 1. For reference, the dynamic (apparent) densities were 4.60 g/cc for Inconel 718 and 2.40 g/cc for Ti-6Al-4V (Ti64), while the solid (particle) densities were 8.20 g/cc and 4.41 g/cc, respectively. SEM images of the Inconel 718 and Ti64 powders are shown in Fig. 1.

Table 1 Particle size distributions for Inconel 718 and Ti64

Powder	D10 (µm)	D50 (µm)	D90 (µm)
Inconel 718	51.73	78.32	113.9
Ti64	50.1	69.8	97.1

2.2 Experimental setup

The rheological behavior of the powders is studied using a Revolution Powder Analyzer (RPA) (Mercury Scientific Inc., Newtown, CT, USA). A drum with an inner radius of 25 mm and a width of 35 mm is used to run the experiment. It is filled with 66 g of Ti64 or 110 g of Inconel 718. The drum is rotated at a constant speed of 0.6 RPM to sustain powder motion within the avalanche regime, where powder is carried up the drum wall and collapses under gravity, causing an avalanche event.

The bulk specific potential energy of the powder charge is extracted as a time-series during 150 avalanche events (see Supplementary Information, Section S3). Here, "energy" refers to specific energy, i.e., the potential energy normalized by sample weight. The energy before and after the avalanche, and their difference, are referred to as break, rest, and avalanche energy, respectively, and serve as system responses during DEM model calibration. The raw experimental avalanche time-series data corresponding to the 150 avalanche events are provided as supplementary material.

The RPA provides various response variables, including changes in potential energy, free surface topography, dynamic repose angles, and packing behavior. These are extracted from the projected shadow of the particle bulk in the drum. For calibration, error minimization may use multiple responses. However, the down-scaling approach is most robust when applied to specific potential energy. While the avalanche angle is commonly used in AM powder analysis, it is excluded from the objective function due to its sensitivity to drum radius.

2.3 Simulation setup

The simulation setup involves spherical particles with a size distribution similar to the real particle size distribution reported in Table 1. SEM images of the particles (Fig. 1) indicate that representing them as spherical in the DEM simulation is considered a valid assumption.

A scaling approach is used to reduce the number of particles in the simulation and thus the computational cost. The radius of the RPA drum (R) is reduced by a factor of 5 to 5 mm in the simulation. The drum width is reduced to 1 mm, which remains significantly larger than the mean

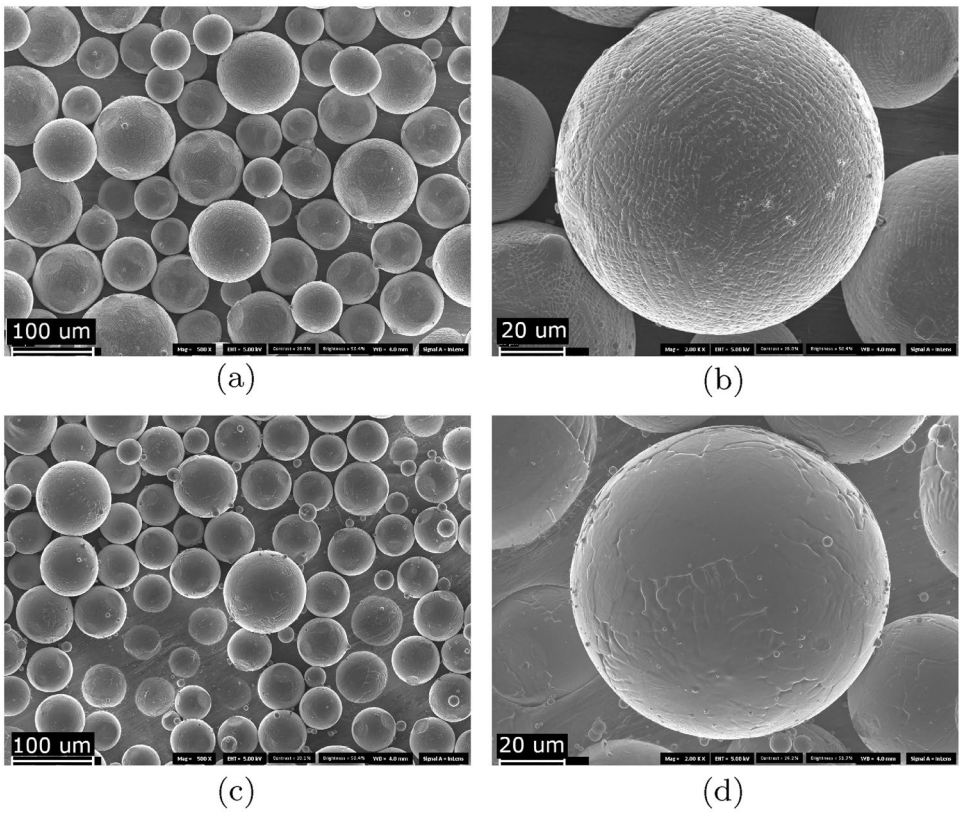

Fig. 1 SEM images of Inconel 718 (**a**, **b**) and Ti64 (**c**, **d**)

particle size of both Ti64 and Inconel 718. The powder weight is scaled with the drum volume to match the experimental filling degree, defined as the volume fraction of the drum filled with powder.

To maintain the balance between gravitational and centrifugal forces, the drum's angular velocity (ω) is adjusted in the simulation to match the experimental Froude number. The Froude number is a dimensionless parameter defined as the ratio of centrifugal to gravitational force based on angular velocity and drum radius [27],

$$Fr = \frac{\omega^2 R}{g} \ , \tag{1}$$

where g is the gravitational acceleration. To preserve the Froude number after reducing the drum radius by a factor of 5, the angular velocity is increased by a factor of $\sqrt{5}$. Accordingly, the experimental angular velocity of 0.6 RPM (period = 100 s) corresponds to 1.34 RPM (period = 44.7 s) in the simulation.

The Ti64 and Inconel 718 simulations include approximately 110,000 and 71,000 particles, respectively. The simulation time step is 0.5 μs, well below the Rayleigh limit and verified to be converged.

2.4 Numerical method

The DEM model is based on step-wise integration of the positions and orientations of the particles according to their properties and interactions with each other and with the environment. For particle i interacting with particle j, the following classical equations of motion apply:

$$(m\ddot{\mathbf{r}})^i = m^i \mathbf{g} + \sum_j \mathbf{f}_{tot}^{ij} \ , \tag{2}$$

$$(I\dot{\omega})^i = \sum_j \mathbf{m}_{tot}^{ij} \ , \tag{3}$$

where m, I, $\mathbf{r}$ and ω are the particle mass, moment of inertia, position, and angular velocity, respectively. $\mathbf{g}$ is the gravitational acceleration, and $\mathbf{f}$ and $\mathbf{m}$ denote force and moment. The operators ($\dot{}$) and ($\ddot{}$) represent first and second time derivatives, respectively. The total force $\mathbf{f}_{tot}^{ij}$ is the sum of the normal and tangential contact forces ($\mathbf{f}_{CN}^{ij}$ and $\mathbf{f}_{CT}^{ij}$) and the normal adhesion component ($\mathbf{f}_{AN}^{ij}$). The total moment is the sum of the rolling resistance moment ($\mathbf{m}_R^{ij}$) and the moment induced by the tangential force:

$$\mathbf{f}_{tot}^{ij} = \mathbf{f}_{CN}^{ij} + \mathbf{f}_{CT}^{ij} + \mathbf{f}_{AN}^{ij} \ , \tag{4}$$

$$\mathrm{m}_{tot}^{ij} = \mathrm{m}_{R}^{ij} + \mathrm{r}_{CG}^{ij} \times \mathrm{f}_{CT}^{ij} \ . \tag{5}$$

Normal and tangential forces include both the elastic and dissipative components and are calculated based on the Hertz-Mindlin-Deresiewicz (HMD) contact model [28]. The force calculations are described in detail in the Supplementary Information, Section S2. A Cartesian grid is used for broad-phase contact detection, followed by a narrow-phase collision search within the local neighborhood. A Verlet velocity predictor-corrector method is implemented for time integration [29].

2.4.1 Rolling resistance

The dissipative tangential force in the original HMD model does not account for the energy dissipated during the rolling motion, which primarily arises from surface roughness and satellite particles. A rolling resistance component is therefore added in Eq. (5) to account for this effect. The rolling resistance torque is defined based on the relative rotational motion of the interacting particles, following [30, 31]:

$$\mathrm{m}_{R}^{ij} = d_R \left\| \mathrm{f}_{CN}^{ij} \right\| r_{eff} \Delta\boldsymbol{\omega}_{\perp} \ , \tag{6}$$

where $\Delta\boldsymbol{\omega}_{\perp} = (\mathrm{I} - \mathrm{n} \otimes \mathrm{n}^T)(\boldsymbol{\omega}_i - \boldsymbol{\omega}_j)$, d_R is rolling resistance coefficient and r_{eff} is the effective radius of the two colliding particles (r_1 and r_2), defined as $1/r_{eff} = 1/r_1 + 1/r_2$.

2.4.2 Adhesion

The adhesion force between particle surfaces can often be neglected for large and dense particles, where gravitational forces dominate. However, for particles with size on the order of tens of microns, adhesion remains a significant factor, even for metallic powders [31]. The dominant source of adhesion in AM powders is the van der Waals (vdW) interaction. The implementation follows the approach proposed by Meier et al. [31]. The vdW force strongly depends on the separation distance between the interacting surfaces. For two surfaces separated a distance δ, the surface energy is given by [32]:

$$\gamma = \frac{A}{24\pi\delta^2}, \tag{7}$$

where A is the Hamaker constant. The normal adhesion force (f_{AN}^{ij}) is defined as the vdW interaction force acting in the normal direction, $F_S(g_N)\mathrm{n}$, and is obtained from [31]:

$$F_S(g_N) = \begin{cases} F_{S0} = -4\pi\gamma r_{eff}, & g_N \le g_0 \\ \frac{A r_{eff}}{6 g_N^2}, & g_0 < g_N < g^* \\ 0, & g_N > g^* \end{cases} \tag{8}$$

with $g_0 := \sqrt{\frac{A r_{eff}}{6 F_{S0}}}$ and $g^* := \frac{g_0}{\sqrt{C_{FS0}}}$, where g_N is the normal gap between the two surfaces. The parameter C_{FS0} defines the transition between the short-range adhesion regime (F_{S0}) and the long-range regime and is set to 1%.

2.5 DEM solver

All simulations are performed using the DEM software Demify® [33]. The Demify® solver has been applied to a wide range of granular material applications, including additive manufacturing [6, 34], railway engineering [35, 36], and heavy machinery [37, 38]. The DEM case implementations are developed using the Demify Python Application Programming Interface (API). The solver utilizes NVIDIA CUDA technology for computation on Graphics Processing Units (GPUs). The computational cluster at the Fraunhofer-Chalmers Centre (FCC) is used for parallel execution of simulation jobs using the Slurm workload manager [39]. Visualization and particle filtering post-processing are performed in the IPS Demify Graphical User Interface (GUI) [33]. The Demify Python API enables case abstraction and advanced post-processing routines, facilitating seamless integration with statistical and optimization packages available in Python. Since a relatively wide range of computational nodes with varying hardware specifications is used in this study, specific performance metrics for individual simulation evaluations are not reported.

2.6 Calibration strategy

Due to the computational cost of DEM simulation, it is desirable to limit the number of simulations required for calibration, a quantity that correlates directly with the number of parameters to be calibrated. Moreover, parameters that do not have a clear and significant effect on powder behavior cannot be reliably identified, making their calibration both inefficient and inaccurate. Therefore, it is crucial to identify the active factors, i.e., parameters that significantly impact the behavior of the powder bulk, prior to calibration. Less influential parameters should be excluded to ensure process efficiency and result accuracy.

The fixed material and interaction parameters used in the calibration are listed in Table 2. Density and Poisson's ratio are treated as intrinsic material properties and assigned based on supplier data. The Young's modulus is reduced relative to the physical material value to ensure numerical stability and manageable computational cost. This practice is established in DEM modeling, as realistic stiffness values

Table 2 Parameter values used in the DEM simulations during the calibration process

Parameter	Value	Ref.
Particle Young's modulus, $E_{particle}$(MPa)	100	–
Particle restitution coefficient, $e_{particle}$	0.4	[31, 42]
Ti64 density, ρ_{Ti64} (kg/m^3)	4400	*
Ti64 Poisson's ratio, ν_{Ti64}	0.33	[43, 44]
Inconel 718 density, ρ_{Inc718} (kg/m^3)	8200	*
Inconel 718 Poisson's ratio, $\nu_{Inconel\,718}$	0.284	[45]
Tool Young's modulus, E_{tool} (MPa)	100	–
Tool Poisson's ratio (steel), $\nu_{particle}$	0.3	[46]
Particle-tool surface energy, γ_{tool} (mJ/m^2)	0.1	**
Particle-tool restitution coefficient, e_{tool}	0.4	[31, 42]
Particle-tool friction coefficient, $\mu_{s,p-t}$	0.4	**
Particle-tool rolling friction coefficient, $d_{R,p-t}$	0.0255	**

*Provided by the producer

**Selected based on the ANOVA analysis (see Sect. 3)

for small particles would require unreasonably small time steps [40, 41]. See Supplementary Information section S1 for a stiffness convergence analysis.

The coefficient of restitution for particle–particle and particle–tool interactions is fixed at 0.4, consistent with values reported for metallic powders [47] and supported by studies demonstrating that restitution has comparatively low influence in dense granular flow regimes, where friction and cohesion dominate energy dissipation [48]. Fixing these parameters reduces the dimensionality of the calibration problem without compromising model fidelity.

The calibration candidate set consists of six variables: friction coefficient, rolling friction coefficient, and van der Waals (vdW) surface energy, each defined separately for particle–particle and particle–tool interactions. DOE is used to assess their influence on system responses. Seventeen parameter combinations are generated: sixteen using a two-level fractional factorial design and one center point representing the midpoint of all factor ranges. The upper and lower bounds for friction, rolling friction, and surface energy are ub = [0.65, 0.05, 0.2 (mJ/m^2)] and lb = [0.1, 0.001, 0.01 (mJ/m^2)]. Simulation responses for these input sets are analyzed using analysis of variance (ANOVA) to identify active factors, significance, and interaction effects. The results indicate that particle–tool interaction parameters have considerably lower influence on the response metrics compared to particle–particle parameters. Therefore, particle–tool friction, rolling resistance, and surface energy are subsequently fixed at the midpoint of their respective ranges in the remaining calibration steps.

A flowchart of the calibration process is shown in Fig. 2. The process begins by establishing the relationship between active factors and responses via a surrogate model. To build

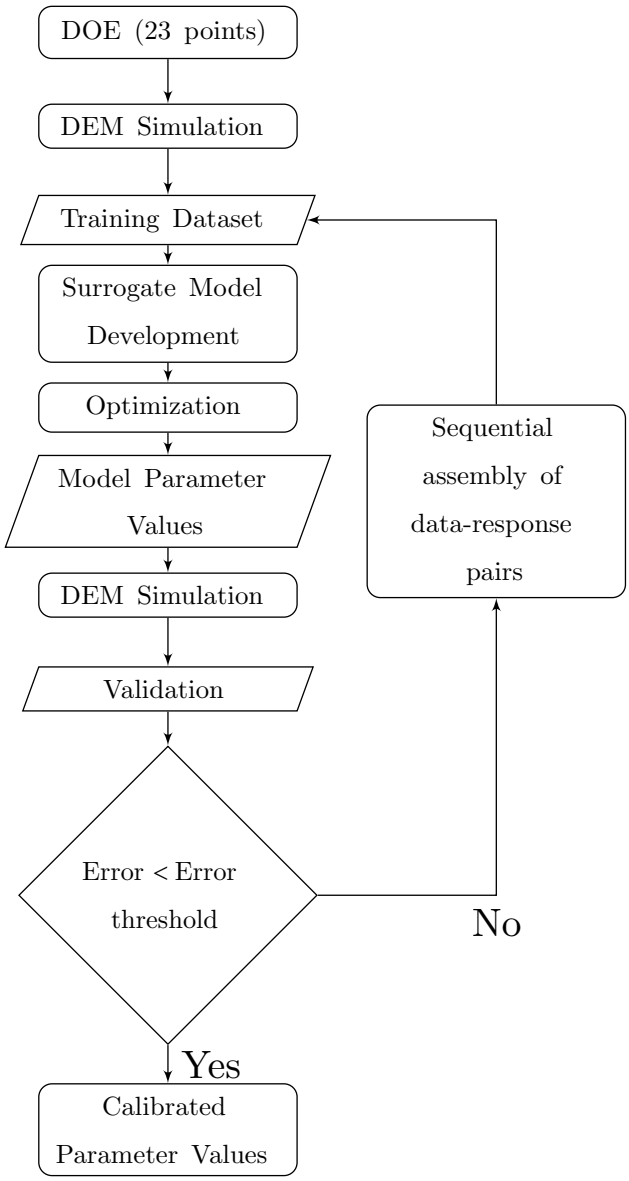

Fig. 2 Flowchart of the calibration process

this model, a 23-point Design of Experiments (DOE) is used, comprising 16 points from a central composite design (CCD) and 7 center-point repetitions. The upper and lower bounds for friction coefficient, rolling friction, and surface energy are ub = [0.65, 0.05, 0.2 (mJ/m^2)] and lb = [0.1, 0.001, 0.01 (mJ/m^2)], respectively. DEM simulations are performed with these parameter sets to generate responses, which, together with the corresponding inputs, form the training dataset. The surrogate model consists of three multi-input single-output polynomials, each corresponding to one response. ANOVA identifies the order and combinations of active factors to include in the polynomials. Polynomial coefficients are determined via response surface fitting using the Ordinary Least Squares (OLS) method.

The surrogate model enables prediction of bulk powder behavior based on specified active factor values. Calibrated parameters are obtained by identifying values that produce responses matching the experimental reference (target responses). An optimization method minimizes the discrepancy between surrogate predictions and target responses. The objective function is defined as follows:

$$\arg\min_{\mathbf{x}\in\mathbb{R}^n} \|f(\mathbf{x})\|_2 \quad \text{s.t.} \quad \mathbf{l} \le \mathbf{x} \le \mathbf{u} \tag{9}$$

where n is the number of parameters to be calibrated, and $\mathbf{l}$ and $\mathbf{u}$ are [0.1, 0.001, 0.01 (mJ/m^2)] and [0.8, 0.5, 0.2 (mJ/m^2)] for the friction coefficient, rolling friction coefficient, and surface energy, respectively, and

$$f(\mathbf{x}) = \begin{bmatrix} \hat{Y}_{BE}(\mathbf{x}) - \bar{Y}_{BE} \\ \hat{Y}_{RE}(\mathbf{x}) - \bar{Y}_{RE} \\ \hat{Y}_{AE}(\mathbf{x}) - \bar{Y}_{AE} \\ \left(\hat{Y}_{BE}(\mathbf{x}) - \hat{Y}_{RE}(\mathbf{x})\right) - \bar{Y}_{AE} \end{bmatrix} \tag{10}$$

$\hat{Y}_{BE}(\mathbf{x}), \hat{Y}_{RE}(\mathbf{x})$, and $\hat{Y}_{AE}(\mathbf{x})$ in Eq. (10) are the mean values of the break, rest, and avalanche energy predicted by the surrogate model and $\bar{Y}_{BE}, \bar{Y}_{RE}$, and $\bar{Y}_{AE}$ are the corresponding target mean values. Because the avalanche energy (AE) is defined as the difference between break (BE) and rest (RE) energy, the fourth element in the 4x1 vector-valued function $f(\mathbf{x})$ is included to ensure that the optimization process properly accounts for the interdependence between BE, RE, and AE. As the objective function is not convex, the derivative-free Powell method is used for optimization.

Note that the optimization is not carried out directly against experimental data, since each DEM evaluation is computationally expensive and would render such an approach intractable. Instead, the surrogate model provides an efficient intermediate representation, and all optimized parameter sets are subsequently validated against the experimental reference responses through DEM simulations. This surrogate-based calibration workflow is standard in domains where high-fidelity simulations incur substantial computational cost.

The optimized parameter values are validated by implementing them in the simulation, running it, and comparing the responses with experimental data. For each response (mean break, rest, and avalanche energy), the error is calculated as the difference between experimental and simulation results. If all three errors are below a predetermined threshold, calibration is finalized and the optimized values are accepted. Significant deviations indicate that the surrogate model is unable to accurately predict simulation outcomes. In that case, the input parameters and simulation responses are added as an additional data point to the training dataset, and the surrogate model is updated. This loop of model development, optimization, and validation is repeated until the exit criteria are met.

The optimization ranges for the parameters are defined based on the literature (Sect. 5). The surface energy and friction coefficients are expected to be around 0.1 mJ/m^2 and 0.4 respectively, according to a study by Meier et al. [31]. An estimate for the rolling friction is obtained using the approach suggested by Brilliantov et al. [31, 49]:

$$d_R \approx \frac{1-e}{1.153}\left(\frac{1-\nu^2}{V_{ref}E\sqrt{r_{eff}/2}}\right)^{1/5}, \tag{11}$$

where e is the restitution coefficient, V_{ref} is the reference velocity, E is the Young's modulus, ν is the Poisson's ratio and r_{eff} is the effective radius of the two colliding particles (r_1 and r_2), defined as $1/r_{eff} = 1/r_1 + 1/r_2$. By setting $r_1 = r_2 = r_{mean}$ and V_{ref} to a value from the upper range of the particle-particle impact velocity, a value close to 2.5×10^{-2} is obtained from Eq. (11) for both Ti64 and Inconel 718 powders. The error threshold for validation of the optimization results is set according to the standard deviation of the experimental data.

3 Results and discussion

A 33 s segment of the measured energy time series for Ti64 and Inconel 718 powders is shown in Fig. 3 (the complete dataset is provided in the Supplementary Information, Section S3). The experimental responses, listed in Table 3, are obtained by averaging the break, rest, and avalanche energies over 150 avalanche events. CV denotes the coefficient of variation, which is defined as the standard deviation divided by the mean value.

The break and rest energies are more than an order of magnitude larger than the avalanche energy, which is defined as their difference. Consequently, small variations in these values can lead to large relative changes in the avalanche energy. As a result, the CV of the break and rest energies is markedly lower than that of the avalanche energy. For both powders, the standard deviation of the break energy exceeds that of the rest energy, indicating that the relatively high variability of the avalanche energy primarily originates from fluctuations in the break energy. This quantitative difference between break and avalanche energies is consistent with the known sensitivity of avalanche-based metrics to small experimental variations and highlights the importance of validating such responses using DEM simulations.

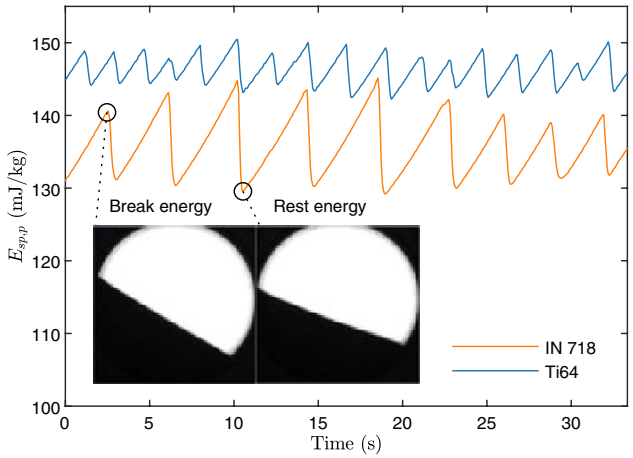

Fig. 3 Measured specific energy (potential energy normalized by the powder mass) time-series for the Inconel 718 and Ti64 powders in RPA. The larger oscillation amplitudes observed for Inconel 718 reflect its higher density and larger particle size compared to Ti64, resulting in greater energy release during avalanches

Table 3 Responses extracted from the RPA measurements

Powder	Ti64	Inconel718
Mean break energy (mJ/kg)	148.86	142.60
Break energy St.Dev. (mJ/kg)	1.14	2.42
CV of break energy (%)	0.77	1.69
Mean rest energy (mJ/kg)	143.26	130.40
Rest energy St.Dev. (mJ/kg)	0.86	1.30
CV of rest energy (%)	0.60	1.00
Mean avalanche energy (mJ/kg)	5.6	12.2
Avalanche energy St.Dev. (mJ/kg)	1.81	3.57
CV of avalanche energy (%)	32.35	29.30

Among the six candidate parameters investigated to identify the active factors, the particle-particle friction coefficient ($\mu_{s,p-p}$), rolling friction coefficient ($d_{R,p-p}$) and particle surface energy ($\gamma_{particle}$) are found to be significant, whereas the particle-tool interaction parameters are not. The non-significant parameters are fixed at the midpoint of the DOE range, as their variation does not have a measurable impact on the responses. The parameter values used during the calibration process are listed in Table 2. The inter-particle and particle-tool parameters without particle material specification in Table 2 are assumed to be identical for both Ti64 and Inconel 718 powders.

The ANOVA results used to determine the terms included in the surrogate models for Inconel 718 and Ti64 powders are shown in Fig. 4 (additional details are provided in the Supplementary Information, Sects. S1 and S2). X1, X2, and X3 denote the friction coefficient, rolling friction coefficient, and surface energy, respectively. The surrogate model comprises three separate polynomials corresponding to the mean break, rest, and avalanche energies. Terms with p-values below the 5% significance level are included.

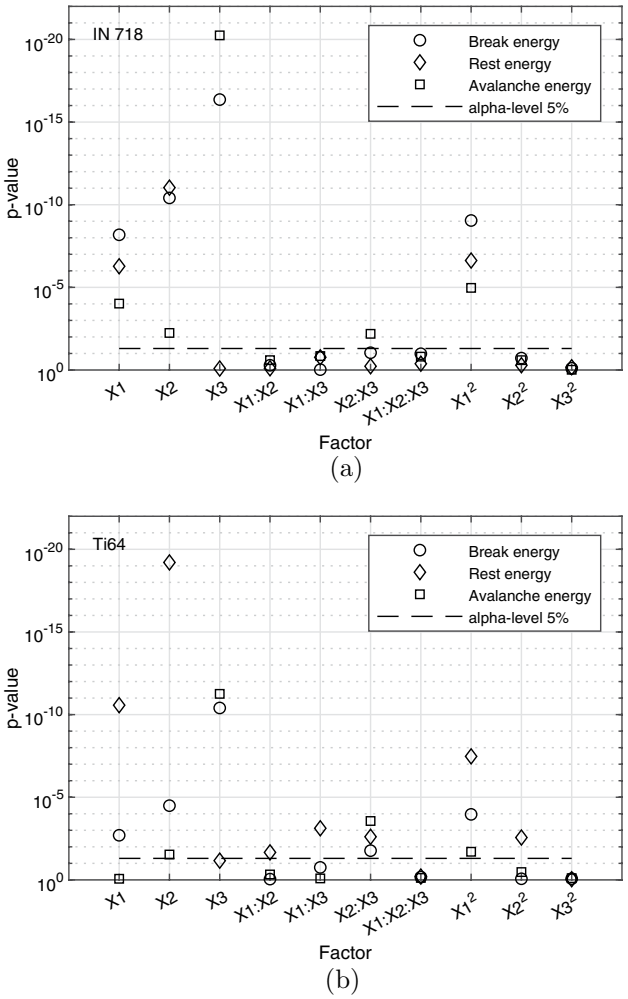

Fig. 4 Plots of p-values from the ANOVA analysis used to identify active factors for the three responses: break, rest and avalanche energy for (**a**) Inconel 718 and (**b**) Ti64. X1, X2, and X3 represent friction coefficient, rolling friction coefficient, and surface energy, respectively. The dashed line indicates the significance level (alpha=5%) When comparing the two powders, the influence of X1 (sliding friction) is stronger for Inconel 718 than for Ti64, consistent with its higher density and larger particle size.

For Inconel 718, the included terms are X1, X2, X3, and $X1^2$ for break energy; X1, X2, and $X1^2$ for rest energy; and X1, X2, X3, X2:X3, and $X1^2$ for avalanche energy. For Ti64, the included terms are X1, X2, X3, X2:X3, and $X1^2$ for break energy; X2, X3, X2:X3, and $X1^2$ for avalanche energy; and all terms except X1:X2:X3 and $X3^2$ for rest energy. Further details are provided in the Supplementary Information.

The results show a notable disparity in how the active factors affect the responses for the two powders, leading to distinct surrogate models. This underscores the importance of powder-specific model calibration. The balance between sliding friction and surface energy differs markedly between the two alloys, reflecting their contrasting material

properties. Inconel 718, with its higher density and larger particle size, exhibits responses dominated by frictional effects, whereas Ti64, with its lower density and finer particle size distribution, shows stronger sensitivity to surface energy. This indicates that frictional resistance governs the dynamics of denser, coarser powders, while cohesive interactions play a larger role in finer, lighter powders, emphasizing the need for powder-specific calibration strategies within a unified framework.

For Inconel 718, the break and rest energies depend primarily on sliding and rolling friction, and the friction–adhesion interaction term (X2:X3) influences only the avalanche energy. For Ti64, friction does not affect the avalanche energy, whereas surface energy influences all responses through the interaction term X2:X3. These trends are consistent with differences in material properties: Inconel 718, with its higher density and larger particle size, is more sensitive to sliding friction than to surface energy compared with Ti64. Similar trends are observed for both powders, where first-order factors dominate over second-order and interaction terms (see Tables S1 and S2 in the Supplementary Information). In addition, surface energy, and thus adhesive forces, has little effect on rest energy but strongly influences break and avalanche energy. The final surrogate models and their adjusted R-squared values are listed in Table S3 in the Supplementary Information.

The calibrated parameter values are obtained by optimizing an objective function defined as the root sum of squares of the differences between the target responses and surrogate model predictions (Eq. 9, Eq. 10). As explained in subsection 2.3, the RPA drum diameter is scaled down by a ratio of 1:5 in the simulation, and the target response values are scaled accordingly when used in the objective function. Based on the experimental results in Table 3, the error threshold is set to 5% to account for variability in the experimental avalanche energy while ensuring acceptable accuracy. For Ti64, 18 additional data points, and for Inconel 718, 19 additional data points are required beyond the initial DOE to refine the surrogate model until it generates calibration parameters that satisfy the termination criterion of the optimization algorithm shown in Fig. 2 (see section S4 for more details).

Final calibrated values for the active factors, along with parameter ranges reported in previous studies on Ni-based and Ti-6Al-4V alloys, are listed in Table 4 and Table 5, respectively. All calibrated values fall within the ranges reported in the literature.

The responses obtained using the calibrated model are compared with the experimental results in Sect. 6. For both powders, the percentage difference between the simulation results and the targets is below the 5% threshold. However, this value is higher for Ti64 than for Inconel 718, possibly due to the low target avalanche energy in the case of Ti64. In general, weaker particle interactions result in higher avalanche energy, as well as higher break energy. The optimizer has identified a parameter set that reduces the avalanche energy to an acceptable level while keeping the break and rest energies within 5% of the target values. In the case of Inconel 718, where the avalanche energy is more than twice as high, this approach yields better optimization results, likely due to the higher target energy and the system's ability to accommodate larger variations without compromising performance.

To facilitate visual comparison, the normalized energy time series are shown in Sect. 5. As explained in subsection 2.3, the geometry is down-scaled and the drum angular velocity is adjusted to maintain the Froude number. Therefore, the energy (y-axis) is normalized by the drum radius and the time (x-axis) by the rotation period, allowing consistent visual comparison between experiments and simulations. Snapshots of break, avalanche, and rest positions from both simulation and experimental measurements are displayed in the insets.

To verify the scaling method, three additional simulations were run with different drum radii. The responses are plotted against the drum radius in Fig. 6. The extrapolated

Table 4 Calibrated parameters values

Powder	Particle friction coefficient	Particle rolling friction coefficient	Particle surface energy (mJ/m^2)
Inconel 718	0.76	0.08	0.16
Ti64	0.78	0.14	0.015

Table 5 Ranges of powder inter-particle interaction parameters reported in studies involving Ni-based and Ti-6Al-4V alloys [23, 31, 42–44, 47, 50–58]

Parameter	Range
Friction coefficient, $\mu_{s,p-p}$	0.12–0.8
Rolling friction coefficient, $d_{R,p-p}$	0.005–0.51
Surface energy, γ_{p-p} $(\mathrm{mJ/m^2})$	0.02–4.87

Table 6 Target values compared with simulation results obtained using the calibrated parameters

	Break energy	Rest energy	Avalanche energy
Inconel 718			
Target (mJ/kg)	28.52	26.08	2.44
Sim. result (mJ/kg)	28.45	26.01	2.441
|Target - Sim. results| (%)	0.22	0.25	0.04
Ti64			
Target (mJ/kg)	29.77	28.65	1.12
Sim. result (mJ/kg)	29.69	28.53	1.16
|Target - Sim. results| (%)	0.25	0.42	3.83

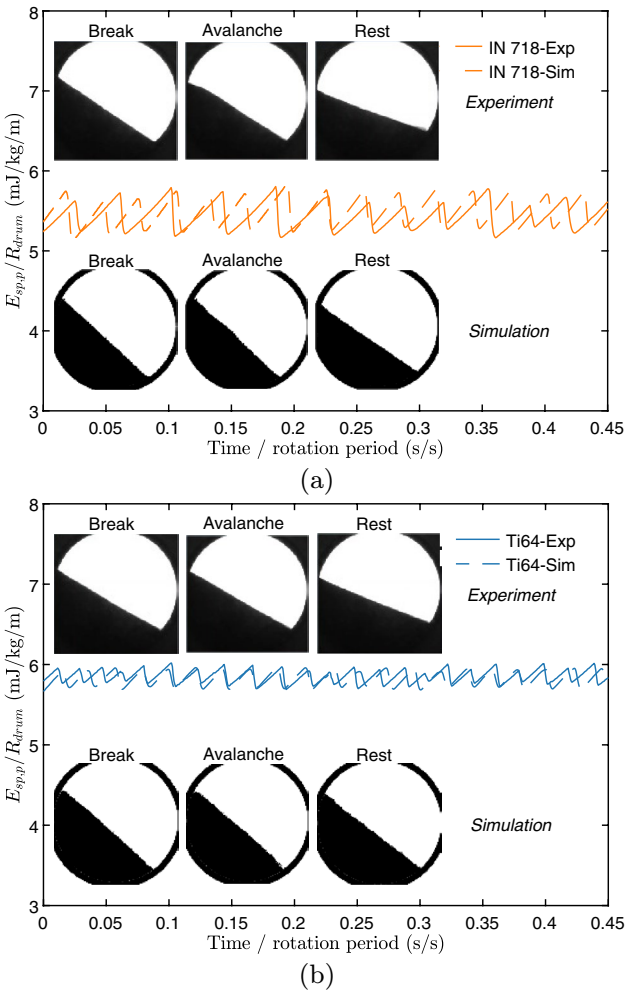

Fig. 5 Comparison of the normalized specific energy (potential energy normalized by powder mass) time-series from experimental and simulated results for (**a**) Inconel 718 and (**b**) Ti64. Time is normalized by rotation period, and energy is normalized by the drum radius. The inset shows snapshots of the break, avalanche, and rest positions from both the simulation and experimental measurements

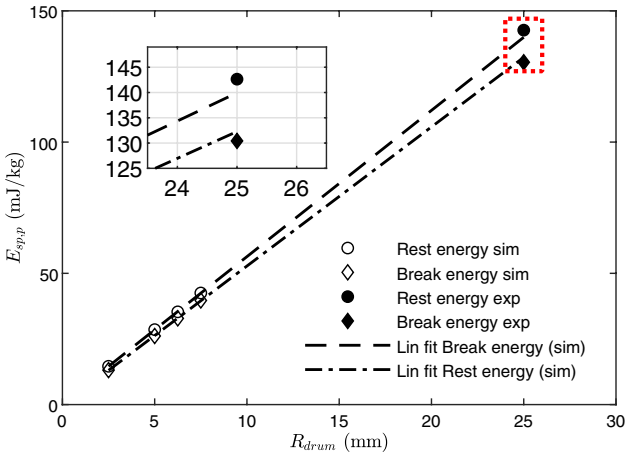

Fig. 6 Simulated break and rest energy versus drum radius, corresponding linear trend lines, and the experimental break and rest energy. The inset shows a magnified section where the extrapolated trend lines reach a radius of 25 mm, corresponding to the radius of the RPA drum, and indicating the predicted energy at this radius. This confirms that the Froude-based down-scaling approach preserves bulk energy responses across drum sizes.

linear trend lines fitted to the simulation results reach the experimental value with approximately 1.8% and 1.42% error for break and rest energy, respectively.

As the drum radius increases from 2.5 to 7.5 mm in the simulation setup, the ratio of average particle size to drum radius varies between 3% and 1%. This ratio and its variation are relatively small, since the geometry is scaled down only to a limit where the drum dimensions remain considerably larger than the particle size. As shown in Fig. 6, this small variation does not affect the linear scaling of the energy with radius.

The DEM visualizations presented in Figs. 7 and 8 serve as a qualitative complement to the energy-based calibration, illustrating that the simulated powder exhibits the expected avalanche behavior observed in the RPA. These snapshots provide mechanistic insight into internal particle rearrangements during an avalanche, which cannot be resolved experimentally from bulk energy measurements alone.

The timeline of an avalanche event is illustrated in Fig. 7. The avalanche typically begins when a few large particles acquire sufficient energy to roll down the surface, colliding with and displacing neighboring particles along their path. In snapshot 3 of Fig. 7, particles near the lower section of the surface begin to roll, destabilizing the support structure for particles positioned higher up. This triggers the propagation of the avalanche toward the upper region, leading to the formation of a shear layer. The avalanche progresses until particles in the lower section of the surface reach a stable, interlocked configuration that prevents further significant displacement by particles rolling from above (as seen in snapshot 8). Eventually, high-energy particles from the top either roll down completely or become trapped along the way, allowing the bulk material to settle into a stable rest position. These dynamics illustrate how localized failures can cascade into full avalanches, a mechanism that parallels the rearrangement of powder under the shear imposed during recoating.

Another phenomenon that is difficult to track experimentally is size segregation. Size segregation is a well-known effect that is often studied in mixing applications [59, 60]. The segregation timeline is illustrated in Fig. 8. During an avalanche event, larger and heavier particles often possess sufficient energy to roll all the way down, while smaller particles are more likely to become trapped along their path, as shown in snapshot 2 of Fig. 8. Following each avalanche, a cluster of large particles accumulates near the lower region

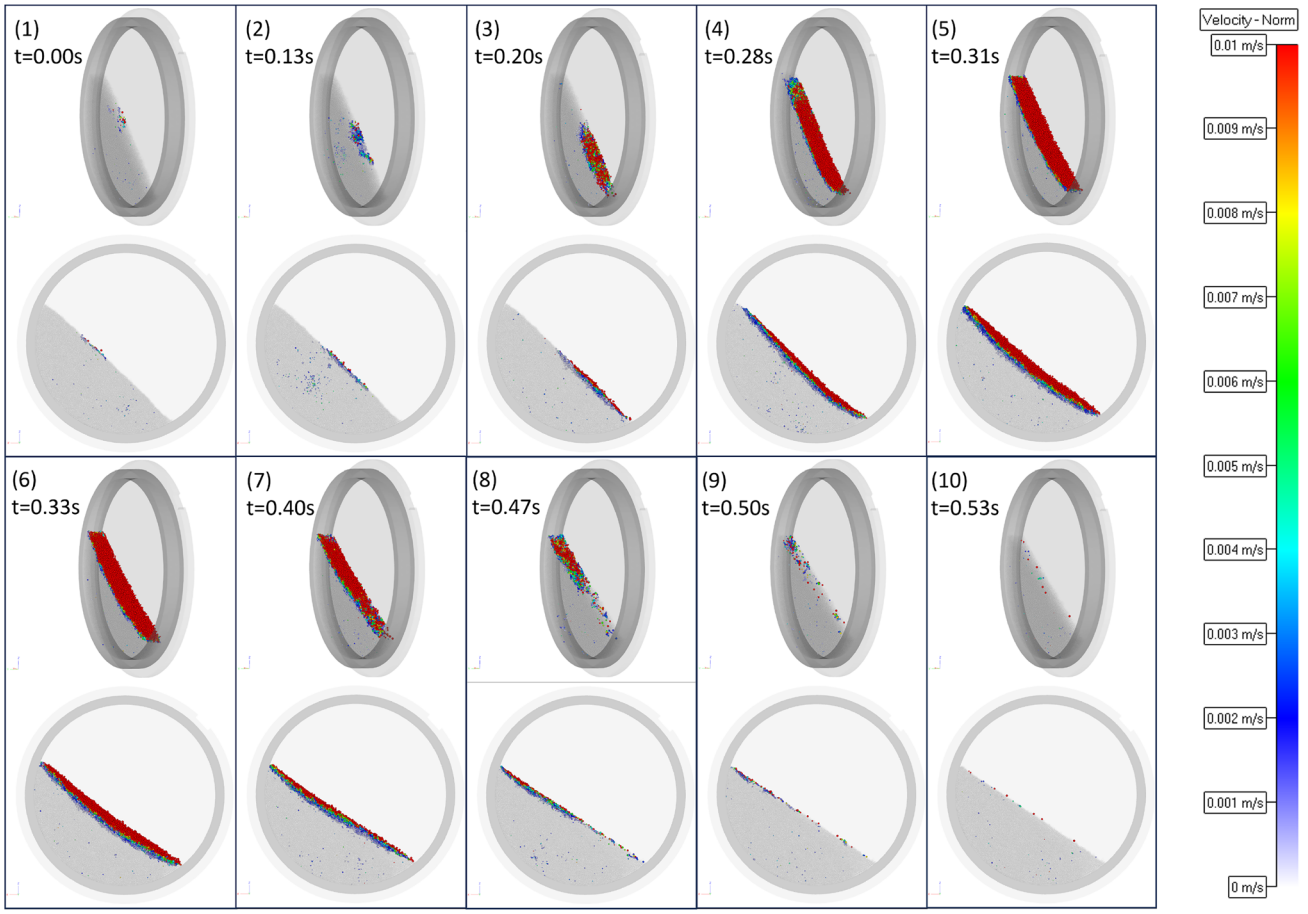

Fig. 7 Time-sequence of snapshots for a characteristic avalanche event. The propagation of motion from a few rolling particles into a shear layer reflects collective dynamics that cannot be captured from bulk energy measurements alone

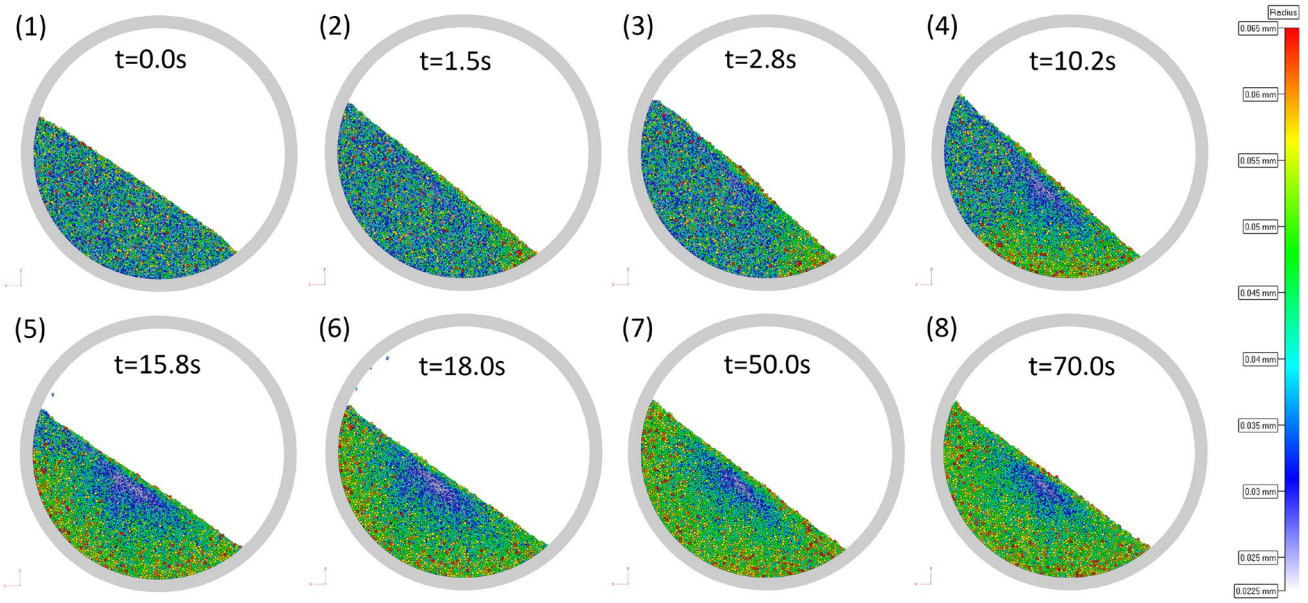

Fig. 8 Particle size segregation in the RPA setup. The migration of larger particles toward the periphery and finer particles toward the core illustrates stratification mechanisms with direct implications for powder-bed homogeneity in AM

of the bulk surface (snapshot 3). With successive avalanche events, this cluster grows and is progressively dragged along the drum wall during rotation. This process initiates size segregation, where larger particles migrate closer to the drum wall (snapshots 3 and 4). As the drum continues to rotate, the segregated larger particles are carried upward along the wall, eventually reaching the upper edge of the bulk surface (snapshot 5). At this point, they roll down during the avalanche, contributing predominantly to the shear layer (snapshot 6). Over time, the size segregation stabilizes, resulting in a configuration where larger particles are mostly located along the drum walls and at the bulk surface, while smaller particles concentrate in the central region of the bulk (snapshots 7 and 8).

The size segregation observed in the drum differs from that in powder-bed recoating, where smaller particles tend to stratify to the bottom of the bed [61]. During avalanching, larger particles roll toward the drum periphery, while smaller ones become trapped along their path and percolate into the core ("kinetic sieving"), forming a fines-rich central "kidney" region. Although the geometry differs from LPBF recoating, these observations demonstrate mechanisms, such as preferential fines concentration, that influence layer uniformity during spreading. In LPBF spreading, horizontal shear from the build plate and recoater blade instead drags and traps fine particles along the walls, as reported in the referenced study.

4 Conclusions

This work presents a Froude-number-based framework for calibrating DEM models for AM powders while retaining the real particle size distribution. The method is demonstrated for two representative PBF-EB alloys, Inconel 718 and Ti-6Al-4V, using a revolution drum setup and the break, rest, and avalanche energies as calibration responses. Calibration is performed using geometrically down-scaled DEM simulations that preserve both particle size and dynamic similarity in terms of the Froude number.

The DOE and surrogate-model analysis indicate that, within the tested experimental and numerical conditions, the dominant contributors to bulk flow behavior are the particle-particle friction coefficient, rolling friction coefficient, and surface energy, whereas particle–tool interactions have limited influence in this specific setup. The optimized parameters fall within ranges reported in the literature, and the distinct parameter sensitivities observed between Inconel 718 and Ti-6Al-4V highlight the need for powder-specific calibration rather than the use of generic values.

Verification of the down-scaling approach across the tested drum sizes shows a linear relationship between bulk energy responses and drum radius, indicating that the method is effective within the investigated range. The calibrated simulations additionally provide mechanistic insight into avalanche development and size segregation, offering value beyond parameter fitting.

Several limitations remain. Preserving only the Froude number does not guarantee full similarity across all relevant dimensionless groups, particularly for cohesive fine powders. Furthermore, the present study focuses on rotating drum flow and does not yet establish a direct quantitative correlation with powder spreading in AM systems.

Further work is underway to investigate scaling effects and assess their transferability to other geometries and powder spreading processes. The goal is to establish a quantitative link between RPA-based calibration and powder layer formation in AM, thereby improving the predictive capability of DEM models under process-relevant conditions. Future work will include experimental validation of scaling laws using newly manufactured drum adapters with multiple diameters, enabling direct comparison between scaled simulations and corresponding RPA measurements. The outcomes are expected to clarify the limits of Froude-based similarity, particularly the influence of wall effects in small-scale geometries. Implementing smaller drums will also facilitate closer alignment between experimental and simulated conditions, although this requires modifications to camera positioning and software configuration.

Supplementary Information The online version contains supplementary material available at https://doi.org/10.1007/s40964-026-01627-6.

Author contributions N.S., J.Q and G.K. wrote the main manuscript. N.S. and J.Q. conducted the simulation studies and data analysis. S.K., G. S. and L.C. conducted the experiments. E.H. led the experimental part of the project. F.E., G.K. and J. Q. led the simulation and data analysis part of the project. All authors reviewed the manuscript.

Funding Open access funding provided by Chalmers University of Technology.

Data availability The raw experimental avalanche time series data generated in this study are provided in the Supplementary Information. All data supporting the findings of this work are available within the article and its Supplementary Information.

Declarations

Conflict of interest The authors declare no Conflict of interest.

References

1. du Plessis A, Yadroitsava I, Yadroitsev I (2020) Effects of defects on mechanical properties in metal additive manufacturing: a review focusing on x-ray tomography insights. Material I& Des 187:108385. https://doi.org/10.1016/j.matdes.2019.108385
2. Talebi FA, Haydari Z, Salehi H, Mehrabi M, Gardy J, Bradley M, Bayly AE, Hassanpour A (2024) Spreadability of powders for additive manufacturing: a critical review of metrics and characterisation methods. Particuology 93:211–234. https://doi.org/10.1016/j.partic.2024.06.013
3. Cordova L, Bor T, de Smit M, Campos M, Tinga T (2020) Measuring the spreadability of pre-treated and moisturized powders for laser powder bed fusion. Addit Manuf 32:101082. https://doi.org/10.1016/j.addma.2020.101082
4. Cundall P, Strack O (1979) A discrete numerical model for granular assemblies. Geotechnique 29(1):47–65. https://doi.org/10.1680/geot.1979.29.1.47
5. Parvanda R, Kala P (2022) Trends, opportunities, and challenges in the integration of the additive manufacturing with industry 4.0. Progr Additive Manuf 8(3):587–614. https://doi.org/10.1007/s40964-022-00351-1
6. Sagar VR, Lorin S, Göhl J, Quist J, Jareteg K, Cromvik C, Mark A, Edelvik F, Wärmefjord K, Söderberg R (2022) A simulation study on the effect of particle size distribution on the printed geometry in selective laser melting. J Manuf Sci Eng 144(5):051006. https://doi.org/10.1115/1.4052705
7. Coetzee C (2017) Review: calibration of the discrete element method. Powder Technol 310:104–142. https://doi.org/10.1016/j.powtec.2017.01.015
8. Coetzee CJ, Scheffler OC (2022) Review: the calibration of dem parameters for the bulk modelling of cohesive materials. Processes 11(1):5. https://doi.org/10.3390/pr11010005
9. Groarke R, Vijayaraghavan RK, Powell D, Rennie A, Brabazon D (2021) Powder characterization-methods, standards, and state of the art, Elsevier, pp 491–527. https://doi.org/10.1016/b978-0-12-824090-8.00006-8
10. Beakawi Al-Hashemi HM, Baghabra Al-Amoudi OS (2018) A review on the angle of repose of granular materials. Powder Technol 330:397–417. https://doi.org/10.1016/j.powtec.2018.02.003
11. Goh HP, Heng PWS, Liew CV (2018) Comparative evaluation of powder flow parameters with reference to particle size and shape. Int J Pharm 547(1–2):133–141. https://doi.org/10.1016/j.ijpharm.2018.05.059
12. Baesso I, Karl D, Spitzer A, Gcommento A, Günster J, Zocca A (2021) Characterization of powder flow behavior for additive manufacturing. Addit Manuf 47:102250. https://doi.org/10.1016/j.addma.2021.102250
13. Neveu A, Francqui F, Lumay G (2022) Measuring powder flow properties in a rotating drum. Measurement 200:111548. https://doi.org/10.1016/j.measurement.2022.111548
14. Hoshishima C, Ohsaki S, Nakamura H, Watano S (2021) Parameter calibration of discrete element method modelling for cohesive and non-spherical particles of powder. Powder Technol 386:199–208. https://doi.org/10.1016/j.powtec.2021.03.044
15. Hu Z, Liu X, Wu W (2018) Study of the critical angles of granular material in rotary drums aimed for fast dem model calibration. Powder Technol 340:563–569. https://doi.org/10.1016/j.powtec.2018.09.065
16. Regis RG, Shoemaker CA (2009) Parallel stochastic global optimization using radial basis functions. INFORMS J Comput 21(3):411–426. https://doi.org/10.1287/ijoc.1090.0325
17. Krityakierne T, Akhtar T, Shoemaker CA (2016) Sop: parallel surrogate global optimization with pareto center selection for computationally expensive single objective problems. J Global Optim 66:417–437. https://doi.org/10.1007/s10898-016-0407-7
18. Liu Z, Yuan J, Shen J, Hu Y, Chen S (2024) A new dem calibration method for wet and stick materials based on the BP neural network. Powder Technol. https://doi.org/10.1016/j.powtec.2024.120228
19. Shentu J, Lin B (2023) A novel machine learning framework for efficient calibration of complex dem model: a case study of a conglomerate sample. Eng Fract Mech 279:109044. https://doi.org/10.1016/j.engfracmech.2023.109044
20. Hadi A, Moradi M, Pang Y, Schott D (2024) Adaptive ai-based surrogate modelling via transfer learning for dem simulation of multi-component segregation. Sci Rep 14(1):27003. https://doi.org/10.1038/s41598-024-78455-7
21. Pantaleev S, Yordanova S, Janda A, Marigo M, Ooi JY (2017) An experimentally validated dem study of powder mixing in a paddle blade mixer. Powder Technol 311:287–302. https://doi.org/10.1016/j.powtec.2016.12.053
22. Richter C, Kunze TR, Katterfeld G, Will A (2020) Development of a standard calibration procedure for the DEM parameters of cohesionless bulk materials - Part II: efficient optimization-based calibration. Powder Technol 360:967–976. https://doi.org/10.1016/j.powtec.2019.10.052
23. Desai PS, Mehta A, Dougherty PS, Higgs CF (2019) A rheometry based calibration of a first-order dem model to generate virtual avatars of metal additive manufacturing (am) powders. Powder Technol 342:441–456. https://doi.org/10.1016/j.powtec.2018.09.047
24. Coetzee CJ (2019) Particle upscaling: calibration and validation of the discrete element method. Powder Technol 344:487–503. https://doi.org/10.1016/j.powtec.2018.12.022
25. Roessler T, Katterfeld A (2018) Scaling of the angle of repose test and its influence on the calibration of dem parameters using upscaled particles. Powder Technol 330:58–66. https://doi.org/10.1016/j.powtec.2018.01.044
26. Feng Y, Owen D (2014) Discrete element modelling of large scale particle systems - i: exact scaling laws. Computat Particle Mech 1:159–168. https://doi.org/10.1007/s40571-014-0010-y
27. Mellmann J (2001) The transverse motion of solids in rotating cylinders-forms of motion and transition behavior. Powder Technol 118(3):251–270. https://doi.org/10.1016/S0032-5910(00)00402-2
28. Mindlin RD (2021) Compliance of elastic bodies in contact. J Appl Mech 16(3):259–268. https://doi.org/10.1115/1.4009973
29. Rozmanov D, Kusalik PG (2010) Robust rotational-velocity-verlet integration methods. Phys Rev E 81(5):056706. https://doi.org/10.1103/physreve.81.056706
30. Luding S (2006) About contact force-laws for cohesive frictional materials in 2D and 3D. Behav Gran Media 9:137–147
31. Meier C, Weissbach R, Weinberg J, Wall WA, Hart AJ (2019) Modeling and characterization of cohesion in fine metal powders with a focus on additive manufacturing process simulations. Powder Technol 343:855–866. https://doi.org/10.1016/j.powtec.2018.11.072
32. Marshall JS, Li S (2014) Adhesive particle flow: a discrete-element approach. Cambridge University Press, Cambridge. https://doi.org/10.1017/CBO9781139424547
33. Industrial Path Solutions, IPS User Manual - Version 2025–R1 - Chapter 18 Demify Particle Simulation (2025)

34. Sani N, Quist J (2023) Calibration of am powders for optimization of recoating applications using dem. In: VIII International conference on particle-based methods (Particles 2023). https://doi.org/10.23967/c.particles.2023.018
35. Eriksson A, Ullrich A, Wang C, Gonzalez-Libreros J, Johansson J, Enoksson O, Quist J, Sas G (2023) Numerical and analytical evaluation of load distribution patterns on ballasted concrete railway bridges. In: A. Ilki, D. Çavunt, Y. S. Çavunt eds International symposium of the international federation for structural concrete, Springer Nature, Cham, pp 109–118. https://doi.org/10.1007/978-3-031-32511-3_12
36. Ullrich A, Quist J, Cromvik C, Jarateg K, Bilock A (2023) A dem-fem coupling framework applied to railroad infrastructure simulations. In: VIII International conference on particle-based methods (Particles 2023)
37. Jahnke J, Steidel S, Burger M, Jareteg K, Quist J (2022) Efficient and robust parameter identification for soil modeled via the discrete element method. In: Berns K, Dressler K, Kalmar R, Stephan N, Teutsch R, Thul M (eds) International commercial vehicle technology symposium, Springer Fachmedien Wiesbaden Wiesbaden, pp 52–63. https://doi.org/10.1007/978-3-658-40783-4_4
38. Ullrich A, Quist J, Cromvik C (2024) A dem-fem coupling approach to model wheel loader bucket loading. In: 11th international conference on conveying and handling of particulate solids (CHoPS 2024), Edinburgh
39. Jette MA, Wickberg T (2023) Architecture of the Slurm workload manager. In: D. Klusáček, J. Corbalán, G. P. Rodrigo (eds) Job scheduling strategies for parallel processing, Springer Nature Cham, pp 3–23. https://doi.org/10.1007/978-3-031-74430-3
40. Paulick M, Morgeneyer M, Kwade A (2015) Review on the influence of elastic particle properties on dem simulation results. Powder Technol 283:66–76. https://doi.org/10.1016/j.powtec.2015.03.040
41. Chen H, Xiao Y, Liu Y, Shi Y (2017) Effect of young's modulus on dem results regarding transverse mixing of particles within a rotating drum. Powder Technol 318:507–517. https://doi.org/10.1016/j.powtec.2017.05.047
42. Han Q, Gu H, Setchi R (2019) Discrete element simulation of powder layer thickness in laser additive manufacturing. Powder Technol 352:91–102. https://doi.org/10.1016/j.powtec.2019.04.057
43. Penny RW, Praegla PM, Ochsenius M, Oropeza D, Weissbach R, Meier C, Wall WA, Hart AJ (2021) Spatial mapping of powder layer density for metal additive manufacturing via transmission x-ray imaging. Addit Manuf 46:102197. https://doi.org/10.1016/j.addma.2021.102197
44. He Y, Hassanpour A, Bayly AE (2021) Combined effect of particle size and surface cohesiveness on powder spreadability for additive manufacturing. Powder Technol 392:191–203. https://doi.org/10.1016/j.powtec.2021.06.046
45. Zhao Y, Cui Y, Hasebe Y, Bian H, Yamanaka K, Aoyagi K, Hagisawa T, Chiba A (2021) Controlling factors determining flowability of powders for additive manufacturing: a combined experimental and simulation study. Powder Technol 393:482–493. https://doi.org/10.1016/j.powtec.2021.08.006
46. Jayaram M (2007) Mechanics of materials: with programs in C, PHI Learning
47. Meier C, Weissbach R, Weinberg J, Wall WA, Hart AJ (2019) Critical influences of particle size and adhesion on the powder layer uniformity in metal additive manufacturing. J Mater Process Technol 266:484–501. https://doi.org/10.1016/j.jmatprotec.2018.10.037
48. Yan Z, Wilkinson S, Stitt E, Marigo M (2015) Discrete element modelling (dem) input parameters: understanding their impact on model predictions using statistical analysis. Computat Particle Mech 2(3):283–299. https://doi.org/10.1007/s40571-015-0056-5
49. Brilliantov NV, Pöschel T (1998) Rolling friction of a viscous sphere on a hard plane. Europhys Lett 42(5):511. https://doi.org/10.1209/epl/i1998-00281-7
50. Dai L, Chan Y, Vastola G, Khan N, Raghavan S, Zhang Y (2021) Characterizing the intrinsic properties of powder – a combined discrete element analysis and hall flowmeter testing study. Adv Powder Technol 32(1):80–87. https://doi.org/10.1016/j.apt.2020.11.015
51. Dai L, Chan Y, Vastola G, Zhang Y (2022) Discrete element simulation of powder flow in revolution powder analyser: effects of shape factor, friction and adhesion. Powder Technol 408:117790. https://doi.org/10.1016/j.powtec.2022.117790
52. Khajepor S, Ejtehadi O, Haeri S (2023) The effects of interstitial inert gas on the spreading of inconel 718 in powder bed fusion. Addit Manuf 75:103737. https://doi.org/10.1016/j.addma.2023.103737
53. Lampitella V, Trofa M, Astarita A, D'Avino G (2021) Discrete element method analysis of the spreading mechanism and its influence on powder bed characteristics in additive manufacturing, Micromachines 12 (4). https://doi.org/10.3390/mi12040392
54. Wang L, Li E, Shen H, Zou R, Yu A, Zhou Z (2020) Adhesion effects on spreading of metal powders in selective laser melting. Powder Technol 363:602–610. https://doi.org/10.1016/j.powtec.2019.12.048
55. Wang L, Yu A, Li E, Shen H, Zhou Z (2021) Effects of spreader geometry on powder spreading process in powder bed additive manufacturing. Powder Technol 384:211–222. https://doi.org/10.1016/j.powtec.2021.02.022
56. Abena A, Aristizabal M, Essa K (2019) Comprehensive numerical modelling of the hot isostatic pressing of ti-6al-4v powder: from filling to consolidation. Adv Powder Technol 30(11):2451–2463. https://doi.org/10.1016/j.apt.2019.07.011
57. Phua A, Doblin C, Owen P, Davies CH, Delaney GW (2021) The effect of recoater geometry and speed on granular convection and size segregation in powder bed fusion. Powder Technol 394:632–644. https://doi.org/10.1016/j.powtec.2021.08.058
58. Shaheen MY, Thornton AR, Luding S, Weinhart T (2021) The influence of material and process parameters on powder spreading in additive manufacturing. Powder Technol 383:564–583. https://doi.org/10.1016/j.powtec.2021.01.058
59. Zuo Z, Wang J, Wu X, Gong S, Zhang J, Lu X (2022) Segregation dynamics of the binary-size granular system in a split rotary drum. Powder Technol 404:117480. https://doi.org/10.1016/j.powtec.2022.117480
60. He S, Gan J, Pinson D, Yu A, Zhou Z (2019) Radial segregation of binary-sized ellipsoids in a rotating drum, Powder Technology, expanding boundaries in particle technology: a select collision of papers from the world congress in particle technology VIII. 357:322–330. https://doi.org/10.1016/j.powtec.2019.08.075
61. Habiba U, Hebert RJ (2023) Powder spreading mechanism in laser powder bed fusion additive manufacturing: experiments and computational approach using discrete element method. Materials. https://doi.org/10.3390/ma16072824
62. Zhou YC, Xu BH, Yu AB, Zulli P (2001) Numerical investigation of the angle of repose of monosized spheres. Phys Rev E 64:021301. https://doi.org/10.1103/PhysRevE.64.021301
63. Combarros M, Feise H, Zetzener H, Kwade A (2014) Segregation of particulate solids: experiments and dem simulations, particuology 12:25–32, special issue on conveying and handling of particulate solids–challenges of discrete element simulation, application and calibration. https://doi.org/10.1016/j.partic.2013.04.005
64. Lommen S, Schott D, Lodewijks G (2014) Dem speedup: stiffness effects on behavior of bulk material, particuology, special

issue on conveying and handling of particulate solids–challenges of discrete element simulation, application and calibration 12:107–112. https://doi.org/10.1016/j.partic.2013.03.006

Authors and Affiliations

Negar Sani[1] · Johannes Quist[1,2] · Sofia Kazi[2] · Gowtham Soundarapandiyan[2] · Gustav Kettil[1] · Laura Cordova[2] · Eduard Hryha[2] · Fredrik Edelvik[1]

✉ Johannes Quist
johannes.quist@chalmers.se

Negar Sani
negar.sani@fcc.chalmers.se

Sofia Kazi
sofiakaz@chalmers.se

Gowtham Soundarapandiyan
gowsou@chalmers.se

Gustav Kettil
gustav.kettil@fcc.chalmers.se

Laura Cordova
laura.cordova@upm.es

Eduard Hryha
hryha@chalmers.se

Fredrik Edelvik
fredrik.edelvik@fcc.chalmers.se

[1] Department of Computational Engineering and Design, Fraunhofer-Chalmers Centre for Industrial Mathematics, Gothenburg, Sweden

[2] Department of Mechanical Engineering, Chalmers University of Technology, Gothenburg, Sweden